Electron transfer between carbon dots and tetranuclear Dawson-derived sandwich polyanions

Antonino Madonia,[1] Alice Sciortino,[2] Mercè Martin-Sabi,[1] Marco Cannas,[2] Souad Ammar,[1] Fabrizio Messina,[2,3] and Delphine Schaming[1,*]*

[1] Université de Paris, ITODYS, UMR 7086 CNRS, 15 rue Jean-Antoine de Baïf, 75013 Paris, France

[2] Università degli Studi di Palermo, DiFC, via Archirafi 36, 90123 Palermo, Italy

[3] Università degli Studi di Palermo, CHAB-ATeN Center, Viale delle Scienze, Edificio 18, 90128 Palermo, Italy

E-mail: delphine.schaming@u-paris.fr; fabrizio.messina@unipa.it

Abstract

Among the photocatalysts which could be used for converting solar energy, polyoxometalates are often regarded as ideal candidates because of their remarkable performances in photocatalytic water splitting and photodegradation of pollutants. Nonetheless, these polyanions are only capable of absorbing UV light, unless coupled to a visible-light photosensitizer. Carbon nanodots are especially promising for this purpose because of their strong visible-light absorption, photostability, non-toxicity, and very low production costs. In this work we demonstrate the possibility of coupling carbon dots to polyoxometalates with different structures, by a simple self-assembly approach based on electrostatic interactions in solution phase. Our studies highlight an extremely efficient interaction between the two compounds, resulting in

ultrafast photoinduced electron or energy transfer from carbon dots to the coupled polyoxometalates, depending on the structure of the latter, as revealed by a detailed study based on ultrafast transient absorption spectroscopy. The evidences herein provided show how nanohybrids based on polyoxometalates photosensitized by carbon dots could find their place in photocatalytic applications, thanks to their remarkable efficiency and huge versatility.

Keywords

Carbon Dots, Polyoxometalates, Charge transfer, Energy Transfer, Fluorescence, Ultrafast Transient Absorption

1. Introduction

With the population growth and the emergence of new economic actors, humanity's impact on the environment is gradually increasing. In particular, the resulting pollution has harmful consequences for the planet. The massive exploitation of fossil fuels in industrialized societies also poses serious environmental problems and ultimately depletes resources.[1,2] In this context, turning to solar energy seems to be one of the most viable solutions. Nevertheless, despite the optimistic premises, solar energy is still not widely used, mostly because we are still unable to efficiently store the harvested energy.[3,4] As a consequence, current research greatly focuses on ways to convert solar radiation into chemical fuel or more generally to use sunpower to catalyze several useful reactions of environmental interest. In particular, the use of nanomaterials for artificial photocatalysis and photosynthesis may offer several routes to address these problems, as for example in the photoinduced decomposition of pollutants or the conversion of water into hydrogen and oxygen.[5–7]

Unfortunately, several useful photocatalysts are only UV-photoactive, a drawback that slows down their possible industrial transfer. A common approach for solving this issue consists in photosensitizing them by coupling to species sensitive to visible light which, once excited by solar radiation, act as charge or energy donors and activate the catalyst. Several compounds such as organic dyes and quantum dots have been already explored in the literature as useful photosensitizers.[8,9] Nevertheless, once again, this strategy

faces several disadvantages because many species used as photosensitizers are either unstable, toxic, or contain rare and expensive metals.

In this context, carbon dots (CDs) appear as ideal candidates for photosensitizing applications. CDs are a novel family of carbon nanoparticles which combine bright fluorescence capabilities, photochemical stability, versatile oxidation/reduction abilities, easy functionalization, bio- and eco-compatibility, and low cost.[10] Moreover, they are able to absorb visible light and were found to be able to readily transfer the absorbed energy or the photoexcited charge carriers to coupled compounds, thus making them possible photosensitizers.[11,12]

On these grounds, this work focuses on the coupling of CDs to polyoxometalates (POMs) with the aim of developing a new family of photocatalytic nanomaterials. POMs are a broad family of polyanionic metal oxide clusters based on transition metals such as molybdenum, tungsten or vanadium in their highest oxidation state. They are known to exchange rapidly and reversibly a large number of electrons, making them very efficient catalysts with applications in a wide array of fields (pollutants degradation, water-splitting…). Concerning photocatalysis applications, like most catalysts, almost all POMs are only active in the UV-domain.[13] In a very recent work, we reported the first evidence of a spontaneous electrostatic coupling between positively charged CDs and a Dawson-type POM, the $[P_2W_{18}O_{62}]^{6-}$ anion.[14] Ultrafast transient absorption spectroscopy allowed to highlight a highly efficient electron transfer within this POM-CDs hybrid, resulting in a charge-separated state formed within 120 fs from photon absorption. Here, we extend this study and explore the coupling of CDs to a wider range of POMs beyond the archetypal $[P_2W_{18}O_{62}]^{6-}$ anion. Indeed, several other POMs with complex structures present more interesting properties, often regarded as very appealing for an applicative transfer. In particular, the POM substituted with transition metal ions are particularly attractive for their possibilities as catalysts.[15] Therefore, we decided to carry out a comprehensive investigation by coupling CDs to two types of tetranuclear Dawson-derived sandwich POMs and analyzing in depth the formation of nano-hybrids through detailed optical measurements. Interestingly, we provide evidence that CDs can be readily coupled to all types of investigated POMs and are capable of behaving as efficient photosensitizers,

capable of excitation transfer to POMs within a few hundreds of femtoseconds from visible-light photoexcitation. Besides, our experimental findings reveal detailed information on the fundamental interaction mechanisms between the two nanomaterials, revealing the existence of both ground- and excited-state interactions between CDs and POMs, and an interplay between photoexcited electron and energy transfer phenomena. The results are interesting in view of the development of a family of photocatalytical active POM-CDs nanohybrids for multiple applications.

2. Experimental section

2.1. Synthesis of CDs

The synthesis procedure of CDs was adapted from the literature.[16] Firstly, 250 mg of crystalline pyrene were crushed down to a powder and then transferred to a flask and dispersed in 20 mL of 70% HNO_3. The pyrene was then nitrated overnight by heating at 80 °C under reflux and vigorous stirring. The resulting 1,3,6-trinitropyrene was recovered as a yellow powder from the solution *via* vacuum filtration and mixed to a 75 mL of 0.4 M ammonia and 1.5 M hydrazine aqueous solution and sonicated for 1 hour. The solution was then transferred into a 125 mL sealed Teflon-lined autoclave which was placed overnight to a 200 °C oven. The CDs were finally separated from unreacted carbonaceous material through vacuum filtration. Finally, the pH of the CDs solution is decreased to 4.0 by HCl additions.

2.2. Synthesis of POMs

Three different polyoxometalate structures were used in this work, namely $K_6[P_2W_{18}O_{62}]\cdot 14H_2O$, $Na_{16}[Co_4(H_2O)_2(P_2W_{15}O_{56})_2]\cdot 51H_2O$, and $Na_{16}[Zn_4(H_2O)_2(P_2W_{15}O_{56})_2]\cdot 50H_2O$; these will be respectively indicated in the course of this article as $\{P_2W_{18}\}$, $\{Co_4P_4W_{30}\}$, and $\{Zn_4P_4W_{30}\}$. All of the treated POMs present either a Dawson or a tetranuclear Dawson-derived sandwich structure. The syntheses of the sandwich POMs were performed from $K_6[P_2W_{18}O_{62}]\cdot 14H_2O$ and $Na_{12}[\alpha\text{-}P_2W_{15}O_{56}]\cdot 24H_2O$, both prepared according the classical method published by Contant.[17] Then the

sandwich POMs were synthesized according a protocol adapted from Finke *et al.*[18] Absorbance spectra regarding the POMs used in this work can be found in the SI (Figure S1).

$K_6[P_2W_{18}O_{62}]\cdot 14H_2O$: 300 g of $Na_2WO_4\cdot 2H_2O$ were dissolved in 350 mL distilled water while stirring. 250 mL of a 4 M HCl solution were next added drop-wise; afterwards, 250 mL of a 4 M H_3PO_4 solution were drop-wise poured as well, before heating under reflux for 24 hours. After cooling, 150 g of KCl were added so to promote formation of a precipitate which was then recovered through vacuum filtration. The dried powder was consequently redissolved in 650 mL distilled water in which I_2 pellets were added to oxidize any reduced W^V centers. After just 10 minutes the I_2 was removed through filtration and the solution was heated at 80°C for 8 days. Finally, the aqueous solution was left to crystallize at 4°C before recovering the $K_6[P_2W_{18}O_{62}]\cdot 14H_2O$ crystals for usage and storage. Yield: 70% (193 g, 40 mmol). ^{31}P NMR (D_2O): $\delta = -12$ ppm.

$Na_{12}P_2W_{15}O_{56}\cdot 24H_2O$: 38.5 g of $K_6[P_2W_{18}O_{62}]\cdot 14H_2O$ was dissolved in 125 mL of water before adding 36.1 g of $NaClO_4$. The aqueous solution was stirred for 20 min before being placed in an ice bath for 3 h. The precipitate formed in the reaction flask was recovered via vacuum filtration and mixed to a 100 mL aqueous solution containing 10.6 g of Na_2CO_3. The solution was stirred for 20 additional minutes before recovering once again the precipitate via vacuum filtration. Once the product was dry, 25 mL of an aqueous solution in which 4 g of NaCl were dissolved in were used to wash the sample. The reaction product was dried in a desiccator before washing it once more with 25 mL of ethanol. The final $Na_{12}P_2W_{15}O_{56}\cdot 24H_2O$ sample was finally recovered and dried under vacuum.

$Na_{16}[Co_4(H_2O)_2(P_2W_{15}O_{56})_2]\cdot 51H_2O$: 365 mg of $Co(NO_3)_2.6H_2O$ (1.125 mmol) was dissolved in 25 mL aqueous solution containing 1 M NaCl and 0.1 M HCl. Then 2.5 g of $Na_{12}[\alpha\text{-}P_2W_{15}O_{56}]\cdot 24H_2O$ (0.56 mmol) were slowly added while vigorously stirring, and the solution turned red as a result. Temperature then was successively increased to 40°C and maintained for 15 min. Afterwards the mixture was left to cool down before adding 2.5 mL of a 1 M NaCl aqueous solution. Finally, the product was left to crystallize in a beaker, and the formed crystals of the final product were recovered after a week. Yield: 83% (3.99 g, 0.46 mmol). ^{31}P NMR (D_2O): $\delta = 6.8$ and 1483 ppm.

$Na_{16}[Zn_4(H_2O)_2(P_2W_{15}O_{56})_2]\cdot 50H_2O$: 160 mg of $ZnCl_2$ (2.175 mmol) was dissolved in 20 mL aqueous solution containing 1 M NaCl. Then 2.5 g of $Na_{12}[\alpha\text{-}P_2W_{15}O_{56}]\cdot 24H_2O$ (2.5 g, 0.56 mmol) were slowly added while vigorously stirring. Temperature was then successively increased to 60°C and maintained for 15 min. Afterwards the mixture was filtered hot and white crystalline solid was collected. Yield: 87% (4.59 g, 0.51 mmol). ^{31}P NMR (D_2O): $\delta = -13.95$ and -3.92 ppm.

2.3. Instruments

Steady-state absorption spectra were obtained on a PerkinElmer LAMBDA spectrophotometer using quartz cuvettes of 1 cm optical path.

Steady-state fluorescence spectra were obtained either on a Horiba FluoroMax-4 spectrofluorometer or on an Aminco-Bowman Series 2 spectrofluorometer using quartz cuvettes of 1 cm optical path.

Time-resolved fluorescence measurements were recorded on an intensified charge-coupled device (CCD) camera while exciting the sample via a tunable laser system. The latter consists of an optical parametric oscillator pumped by a Q-switched Nd:YAG laser (5 ns pulses at 10 Hz repetition rate). The energy of each laser pulse was on average equal to 0.1 mJ and the spectral resolution of the setup was equal to 4 nm. The laser beam is generated at 1064 nm before being converted to a wavelength chosen between 410 and 2400 nm via three non-linear crystals, and then it passes through a polarizing filter. Emission from the sample is collected through a slit and directed towards a diffraction grating (λ_{blaze} = 300 nm, 150 lines/mm) by optical lenses. As the grating has a spectral resolution of 20 nm mm^{-1}, slit aperture was set to 250 µm so to achieve a resolution of 5 nm. The dispersed sample emission spectrum is thus recorded by the intensified CCD camera at a certain delay from the laser pulse, selected thanks to a trigger signal sent by a programmable timing generator, and for a fixed time window of 0.5 ns. The spectral evolution can then be obtained by repeating measurements at different delays from excitation. Cuvettes of 1 cm optical path quartz were used throughout the procedure, filled with a sample solution displaying an absorbance approximately equal to 0.1 at the excitation wavelength so to avoid inner filter effects. Obtained data was treated by removing from each spectrum a linear baseline intercepting points

where no emission signal was present. In addition, to obtain the time traces, intensities in an interval of 10 nm around the chosen wavelength were averaged together so to reduce noise.

Sub-nanosecond **transient absorption measurements** were performed on a laboratory-made setup, based on a 5 kHz Ti:sapphire femtosecond amplifier (Spectra Physics Solstice-Ace) able to produce 75 fs pulses peaking at 800 nm (FWHM = 30 nm) at 700 μJ per impulse. The produced beam is split in two parts by a beam splitter (80% / 20%) to generate the pump and the probe, respectively. On the pump arm, the 800 nm beam is frequency-doubled (type I phase-matching) by an ultrathin β-BBO crystal (250 nm) in order to create a 400 nm beam (20% efficiency), which is then isolated from the fundamental by a Schott BG40 filter. The beam is afterwards chopped at 2500 Hz and focused on the sample using a parabolic mirror with a focal length equal to 150 mm. The polarization of the pump is controlled by a waveplate. On the second arm, white light is generated focusing the 800 nm beam in a 1 mm quartz cuvette containing D_2O so to generate a broadband pulse extending from 400 to 700 nm. The probe is focused on the sample by the same parabolic mirror used to focus the pump. The pump-probe delay in controlled by a motorized delay stage. The probe and the pump overlap within the sample, which continuously flows in a 200 μm thick flow cell upon the action of a peristaltic pump. The flow is regulated so that every pump pulse hits a fresh portion of the sample. After traversing the sample, the probe beam is dispersed through a Brewster-angle silica prism and focused on the detector by a lens. The spectral resolution of this configuration is 3 nm at 550 nm. The temporal resolution is about 120 fs. The dispersed probe beam is revealed by a 1024 pixels detector system (Glaz Linescan-I) with single-shot capability. A typical signal is obtained by averaging 5000 pumped and 5000 unpumped spectra for each delay, and scanning over the pump-probe delay 10-20 times. The concentration of the measured CDs solutions were equal to 2.5 g L^{-1} in order to have an absorbance equal to 0.3 at 400 nm through the flow cell optical path. The measurements were performed in linear regime with an energy of about 100 nJ per pulse. All measurements were carried out under the so-called magic angle detection conditions, so that they are not affected by rotational diffusion or depolarization dynamics.

Dynamic light scattering (DLS) and ζ-potential measurements were carried out on a Malvern Nano ZS model ZEN3600. When measuring hydrodynamic radious R_h, measurements were performed using disposable plastic cuvettes containing 1 mL of sample solution. Results were repeated at different concentrations in order to ensure no sample interaction in solution. DLS size was obtained from the weighted average of the number distribution plot. ζ-potential measurements were performed in an appropriate disposable plastic cuvette. Reported potential distributions were calculated by applying the Henry equation to the electrophoretic mobility of the sample measured in solution using laser doppler velocimetry. Indicated ζ-potential values were obtained by least-squares fitting the charge distribution data with a Gaussian function.

High resolution transmission electron microscopy (HRTEM) measurements were performed on a JEOL JEM-2100F Field Emission Electron Microscope. TEM samples were prepared by depositing several drops of sample solution on a FCF200-Cu grid, by drying between each deposition with paper tissues.

Fourier-transform infrared spectroscopy (FTIR) measurements were performed on a Thermo Scientific spectrometer model IR-TF Nicolet iS10. FTIR samples were prepared by mixing a few drops of CDs solution with 100 mg KBr powder. The wet powder was then mixed and left to dry in air before compressing in order to obtain a pellet. A KBr pellet was used to measure the background. All spectra were acquired by averaging together 50 independent measurements. FTIR spectra were treated via the Thermo Fisher Scientific OMNIC 9 application by subtracting a baseline.

3. Results and discussion

3.1. Structural characterization of CDs

FTIR characterization was performed on CDs in order to analyze their surface composition. Several signals associated to amine moieties, and a minor contribution from hydroxyl groups, were observed in the obtained spectrum (Figure 1A). In our experiment, the pH of CDs solution is decreased to 4.0 in order

to allow electrostatic interactions between CDs and negatively-charged polyanionic POMs: in fact, these acidic conditions lead to the protonation of amine groups into ammonium, allowing CDs to display a net positive charge on their surface. This has been verified by measuring the ζ-potential distribution of an aqueous CDs' solution at the aforementioned pH conditions (Figure 1B) which yields an indication of the average nanoparticles' surface potential.

The structural characterization of CDs was further carried out by electron microscopy measurements. HRTEM images of the sample show small crystalline particles sized around 5 nm (Figure 1C). The Fourier Transform (FFT) of said images was thus calculated in order to obtain further insight on the particles' core structure (Figure 1D). Several well-defined reflections are seen in the resulting pattern, in particular those corresponding to 2.1 and 2.5 Å reticular distances, which can be, in a first lecture, indexed as the (1 0 0) and (0 0 4) reflections of the graphite R-3m structure (ICDD n°98-003-1829). Unfortunately, within this structure, the third measured distance, namely 2.9 Å, did not match with any reflection, even the forbidden ones, forcing us to propose an alternative structural hypothesis, that a nitrated graphite R-3m structure (ICDD n°98-002-8418), with almost the same *a* and *b* unit cell parameters ($a = b \approx 2.46$ Å) but a longer *c* one (53.50 Å instead 10.04 Å). Within this hypothesized structure the observed reflections can be fully indexed as (1 0 0), (0 0 21) and (0 0 18) respectively. Considering the synthesis conditions of the studied CDs, it is not at all excluded that the produced carbon-based matter is much more consistent with a nitrated graphite phase than a pure graphite one.

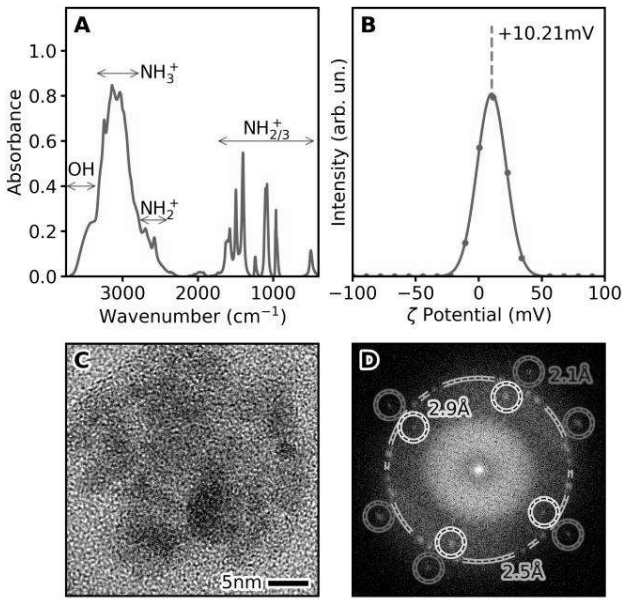

Figure 1: A) FTIR spectrum of CDs and identified vibrational peaks; B) ζ-potential distribution of CDs and relative best-fitting Gaussian curve; C) HRTEM image of several CDs and D) its FFT image.

3.2. Optical measurements

Firstly, we studied the interaction between POM and CDs by steady-state spectroscopic techniques. In particular, the optical characterization was initially performed by observing the effect of POMs on the CDs absorbance in solution. In particular, our experiments focused on the interactions of CDs with three different POMs, $\{P_2W_{18}\}$, $\{Zn_4P_4W_{30}\}$ and $\{Co_4P_4W_{30}\}$. As observed in Figure 2A, 2B and 2C for $\{P_2W_{18}\}$, $\{Zn_4P_4W_{30}\}$ and $\{Co_4P_4W_{30}\}$ respectively, the absorbance bands of CDs (represented by a blue curve) redshift upon addition of the POMs. Furthermore, the interaction with POMs leads to an increase of the absolute absorption intensity, as shown in Figure S2 where non-normalized spectra were plotted.

Considering that absorbance spectroscopy probes transitions from the ground state, these differences suggest an intense ground-state interaction between POMs and CDs, indicating the formation of a nanohybrid whose components display a strong mixing between energy levels of the two species, with consequent changes of both the energy position and intensity of the transitions. When CDs are coupled to either $\{P_2W_{18}\}$ or $\{Zn_4P_4W_{30}\}$, it can be safely concluded that the shift is not merely an apparent effect due to the additional absorption of POMs, as the absorption bands of these polyoxometalates (shown in

Figure 2 as red curves) only contribute below 400 nm. When considering the effects induced by $\{Co_4P_4W_{30}\}$, the situation is complicated by the fact that these POMs display significant absorption also at longer wavelengths. Indeed, as shown in Figure 2C, the signal measured at low concentrations of $\{Co_4P_4W_{30}\}$ (1.25 μM) presents a situation very similar to that observed for the other polyoxometalates: CDs absorbance undergoes a redshift, which evidences once again formation of complexes between $\{Co_4P_4W_{30}\}$ and CDs. Nonetheless, at higher $\{Co_4P_4W_{30}\}$ concentrations (12.5 μM), a very intense band covers almost completely the original CDs absorbance peaks. This could be explained by the fact that $\{Co_4P_4W_{30}\}$ absorbs at longer wavelengths compared to other POMs, up to approximately 450 nm. As a consequence, differentiating POM contributions from changes inherent to the absorbance of CDs is more difficult in this case. Nonetheless, as shown in Figure S2 where we report non-normalized absorption spectra, the observed changes in the spectrum of CDs cannot be entirely explained by the additional contributions due to $\{Co_4P_4W_{30}\}$, pointing to significant interactions also in this case.

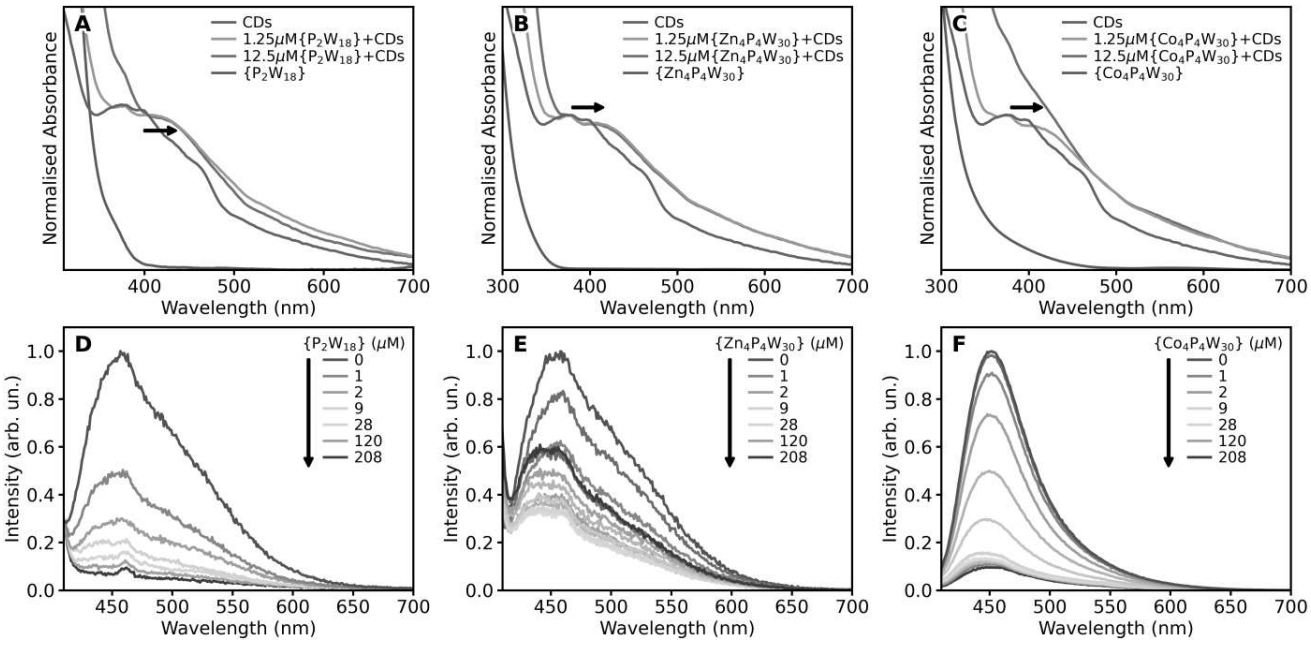

Figure 2: The effects of the interaction between CDs and POMs on CDs optical properties. A, B and C) Absorbance spectra of aqueous solution of CDs (blue line), POMs (red line), and CDs after addition of POMs at two different concentrations (yellow and green lines); spectra have been arbitrarily normalized.

D, E and F) Photoluminescence spectra of CDs (λ_{exc} = 400 nm) quenched by the presence of POMs. Reported effects are due to $\{P_2W_{18}\}$ (A and D), $\{Zn_4P_4W_{30}\}$ (B and E), and $\{Co_4P_4W_{30}\}$ (C and F).

Following these results, the characterisation was deepened by observing how the fluorescence emission intensity of CDs responded when POMs were added in solution. Increases in polyoxometalate concentration progressively cause a quenching of CDs emission, as shown in Figure 2D, 2E and 2F for $\{P_2W_{18}\}$, $\{Zn_4P_4W_{30}\}$ and $\{Co_4P_4W_{30}\}$ respectively. Interestingly, at concentrations of $\{Zn_4P_4W_{30}\}$ above 20 μM the reverse effect is instead observed: consequent increases in concentration appear to gradually restore the photoluminescence band intensity.

The steady state photoluminescence results have been studied through Stern-Volmer plots (*i.e.* the ratio between initial intensity I_0 and intensity I as a function of quencher concentration), shown in Figure 3A. Data relative to $\{P_2W_{18}\}$ seem to clearly indicate that two different quenching processes can be found in the probed range of concentrations, giving rise to two different linear slopes, in the ranges above and below 20 μM, respectively. Also, in the presence of $\{Zn_4P_4W_{30}\}$ we observe at low concentrations a steep linear range associated to the quenching. Above 20 μM, instead, a slowly decreasing curve indicates a partial emission recovery, as already noted above. Finally, in the case of $\{Co_4P_4W_{30}\}$ additions to the solution of CDs, the result is a little bit different, since only a progressive quenching is observed even at high concentrations in POM, until a saturation is reached at around 100 μM.

Least-squares fitting procedures have been performed on the data relative to all POMs, so to obtain further information useful to compare the magnitudes of each process. The following model function has been used:[19]

$$\frac{I_0}{I} = \left[\frac{1 + K[POM]}{1 + K[POM](1 - f)}\right]$$

In this equation, I_0 represents the initial emission intensity, I the intensity at POM concentration equal to $[POM]$, K is the quenching coefficient, which thus expresses the coupling reaction equilibrium constant, and f is an accessibility factor indicating the fraction of CDs accessible to the POM.

As above a 20 μM threshold $\{Zn_4P_4W_{30}\}$ cause a partial recovery of the emission, rather than a quenching, the data relative to this interval has been excluded from the fit for this POM. The obtained quenching constants, for $\{P_2W_{18}\}$, $\{Zn_4P_4W_{30}\}$ and $\{Co_4P_4W_{30}\}$ respectively, are $(24 \pm 7)\times10^5\ M^{-1}$, $(20 \pm 5)\times10^5\ M^{-1}$ and $(9.6 \pm 1.7)\times10^5\ M^{-1}$ with accessibility constants equal to 82.0 ± 1.4%, 70.0 ± 1.4% and 89.9 ± 0.4%, respectively. Therefore, all three POMs display comparable, and rather large, interaction efficiencies with our CDs, as the obtained values express the ability of POMs to quench 50% of CDs emission already at few micromolar concentrations. Regarding the process occurring at $\{P_2W_{18}\}$ concentrations higher than 20 μM, a quenching constant of $(55.4 \pm 1.0)\times10^2\ M^{-1}$ has been obtained and the process does not appear to be limited by an accessibility constant, as evident from the absence of any tendency to saturation.

Diffusion-limited quenching coefficients have been calculated for comparison from the Smoluchowski equation, from the known sizes of CDs and POMs (Table S1 and Figure S3). The highest of these coefficients was found to be equal to 271 ± 12 M^{-1}: as the quenching constants found experimentally are orders of magnitude higher than this value, collisional quenching due to the Brownian motion of POMs and CDs in solution can be safely ruled out as the cause of the observed results. We can thus conclude that diffusional processes are not occurring and that the interactions between CDs and POMs are purely static, that is, CDs fluorescence is quenched upon the formation of stable nanohybrids, as already suggested from optical absorption data revealing ground-state interactions between the two species. In this sense, the quenching constants obtained by the fit can be interpreted as bimolecular rates for the binding reaction CD+POM → [CD–POM]. The bulkier $\{Zn_4P_4W_{30}\}$ and $\{Co_4P_4W_{30}\}$ POMs display a single linear trend in the Stern-Volmer plot, consistent with their attachment to a specific surface group, most likely $–NH_3^+$, in a well-defined geometric configuration. However, at high concentrations we observe saturation of the binding site. The observation of two binding constants for the $\{P_2W_{18}\}$ suggests a second accessible site on the CDs surface, on which only these POMs are able to bind to, possibly because of their smaller size, which also appears to prevent saturation.

Regarding the recovery of the fluorescence intensity observed in the second range (concentrations higher than 20 μM) of the $\{Zn_4P_4W_{30}\}$ Stern-Volmer plot, this result seems unexpected. However, previous studies showed that the interaction of CDs with ions in aqueous solution can screen the nanoparticles from the solvent-related effect, thus causing an increase in the emission intensity of CDs.[20] Thus, we believe that what herein observed is a manifestation of this same effect: while at low concentrations interaction between $\{Zn_4P_4W_{30}\}$ and CDs results in a quenching of fluorescence, above a threshold further coupling between the two species has a screening effect from the solvent interactions, which would otherwise reduce the CDs quantum yield. It is possible in principle that also in the case of $\{P_2W_{18}\}$ and $\{Co_4P_4W_{30}\}$ we have a similar screening but the lack of evidence in the data suggests it to be negligible, maybe because of the lower ionic charge.

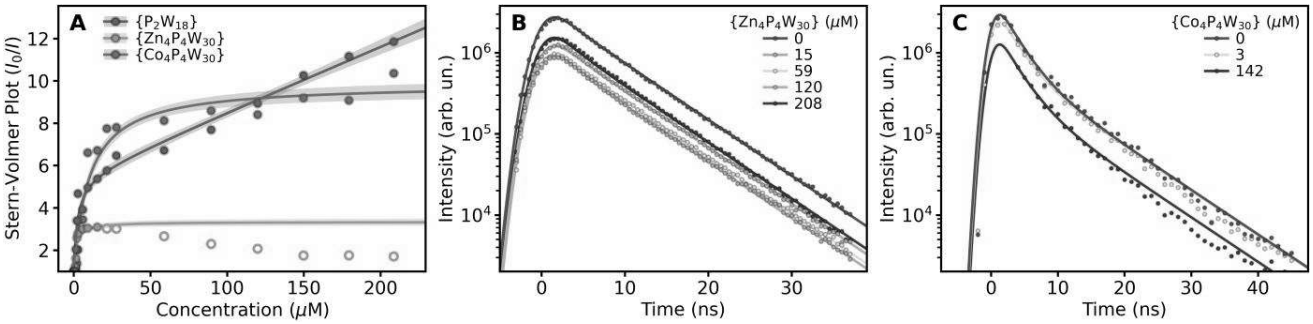

Figure 3: A) The quenching of CDs photoluminescence due to POMs presence shown in a Stern-Volmer plot; continuous lines represent the obtained best-fitting curves as obtained via least-squares fitting procedures; relative 1-σ confidence intervals are shown. Hollow points have been excluded from the fitting procedure, as relative to an intensity increase instead of a quenching. B and C) Time resolved photoemission traces of CDs ($\lambda_{exc} = 450$ nm, $\lambda_{em} = 520$ nm) obtained at different concentrations of $\{Zn_4P_4W_{30}\}$ (B) and $\{Co_4P_4W_{30}\}$ (C).

In order to conclusively confirm that the observed quenching processes are purely due to static interactions between CDs and POMs, time resolved photoluminescence spectroscopy has been used to study the decay kinetics of the nanoparticles's emission in the presence of different concentrations of

quencher. Nanosecond decay traces obtained in the presence of $\{Zn_4P_4W_{30}\}$ and $\{Co_4P_4W_{30}\}$ are respectively shown in Figure 3B and 3C, while those relative to $\{P_2W_{18}\}$ have been previously published.[14] Whatever the POM used and regardless its concentration, the fluorescence decay curves appear to proceed in a parallel manner when plotted on a logarithmic *y*-scale, thus implying a constant decay lifetime. Such a consideration is confirmed by performing a global least-squares fitting procedure on the traces using a bi-exponential decay function as model; this procedure does in fact show that all decay kinetics are described by the same two lifetimes, equal to 6.27 ± 0.05 ns and 2.07 ± 0.14 ns, regardless of POMs presence. This lack of changes proves that the observed quenching is caused by formation of static $\{P_2W_{18}\}$-CDs, $\{Zn_4P_4W_{30}\}$-CDs, and $\{Co_4P_4W_{30}\}$-CDs complexes. Indeed, it is known that this type of interaction does not lead to changes in the nanosecond decay lifetime because the residual fluorescence observed after quenching is only due to the fraction of CDs which have not formed a complex with POMs, and thus display an unchanged lifetime.[19] From another point of view, such a result implies that the inherent time scale of the quenching interaction is in the sub-nanosecond range. In contrast, we can conclusively exclude the eventuality of a dynamic (collisional) quenching which would cause the emission decay kinetics to proceed with a lifetime shorter than that measured in absence of quencher, and progressively decreasing with quencher concentration.

3.3. Sub-nanosecond time-resolved investigations

In order to further understand the mechanism underlying the observed quenching we studied the samples via ultrafast transient absorption (TA) spectroscopy pumped under the irradiation from a 400 nm femtosecond pulsed laser. We use as observables the known TA signals of CDs in the visible range,[14] and monitor their changes in the presence of polyoxometalates at concentrations of 1.25 μM and 125 μM. These values were chosen in order to probe two different regions in the Stern-Volmer plot (Figure 3A).

TA spectra at different delays from the excitation pulse are shown in Figure 4A–D for CDs in absence of POMs, and in the presence of 1.25 μM $\{P_2W_{18}\}$, 1.25 μM $\{Zn_4P_4W_{30}\}$ and 1.25 μM $\{Co_4P_4W_{30}\}$. The data obtained at higher POM concentrations are shown in the SI (Figure S4).

The observed signals share several common features: in all cases the tail of a negative ground state bleaching (GSB) signal peaking outside of the studied region is observed below 440 nm. Most of the remaining wavelengths are covered by an intense and broad excited state absorption (ESA) signal, composed of two different bands peaking around 460 nm and 570 nm. Lastly, a stimulated emission (SE) band can be recognized as a clear dip overlapping the ESA signal at a wavelength of approximately 500 nm. The overall shape of the TA signal, arising from the combination of these signals, undergoes significant changes from sample to sample. For example, the GSB signal in the presence of $\{Zn_4P_4W_{30}\}$ POMs remains obviously more pronounced at all delays from excitation, while decaying to almost zero in bare CDs. Besides, the dip around 500 nm associated to the SE becomes much weaker in the presence of POMs, especially at higher concentrations (Figure S4).

The TA dynamics can be more quantitatively characterized by decay traces taken at representative wavelengths, as shown in Figure 4E, 4F, 4G, and 4H, respectively for the samples in absence of POMs, in the presence of 1.25 μM $\{P_2W_{18}\}$, in the presence of 1.25 μM $\{Zn_4P_4W_{30}\}$ and in the presence of 1.25 μM $\{Co_4P_4W_{30}\}$. Multi-exponential decay curves best describing the data are also shown; these have been obtained via a global least-squares fitting procedure performed simultaneously on the seven datasets acquired on bare CDs, $\{P_2W_{18}\}$-CDs (1.25 μM and 125 μM), $\{Zn_4P_4W_{30}\}$-CDs (1.25 μM and 125 μM) and $\{Co_4P_4W_{30}\}$-CDs (1.25 μM and 125 μM) samples. In particular, the first four *Eigentraces* of the TA data matrixes obtained from their singular value decomposition (SVD) have been used for the fit. This procedure, explained in detail elsewhere,[14] allows to analyze the decaying components present in the transient absorption data and find the time constants associated to their kinetics. In our case, it was found that it is possible to describe all seven datasets with a multi-exponential decay presenting four lifetimes shared by all samples. Three of these lifetimes (0.11 ± 0.02 ps, 1.06 ± 0.17 ps and 20 ± 3 ps) are associated to the dynamics occurring during the probed delays from excitation, while the fourth (> 1 ns) represents signals that live longer than the probe ultrafast dynamics.

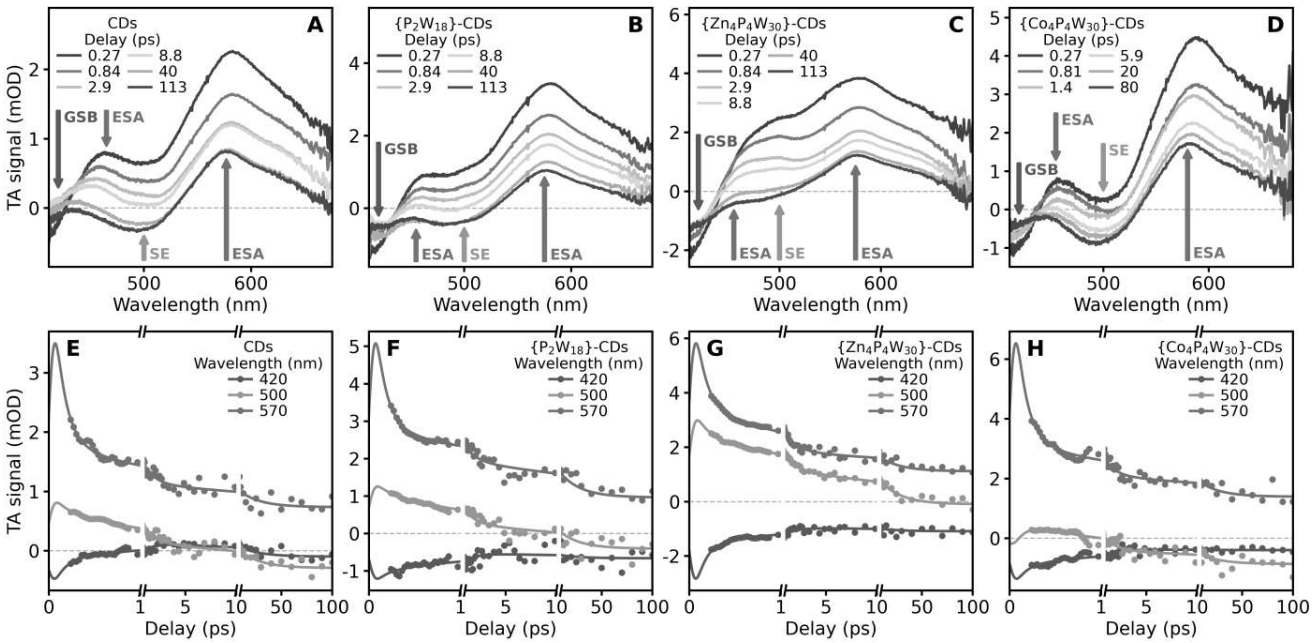

Figure 4: Ultrafast transient absorbance spectra at different delays from excitation (A, B, C and D) and traces taken at different wavelengths (E, F, G and H) of a CDs solution excited by a 400 nm femto-second laser pulse, either in the absence of POMs (A and E), in the presence of 1.25 µM of $\{P_2W_{18}\}$ (B and F), in the presence of 1.25 µM of $\{Zn_4P_4W_{30}\}$ (C and G) or in the presence of 1.25 µM of $\{Co_4P_4W_{30}\}$ (D and H). The best fitting multi-exponential decay curves obtained via a global least-squares minimization procedure are overlapped on the data.

The SVD analysis also yields the decay associated spectra (DAS), describing the TA spectral signatures associated to the different temporal components. The DAS for all the samples are shown in Figure 5. Their shapes are slightly different from sample to sample, which is not surprising considering the differences already observed in linear steady-state absorption. However, they follow a general trend which can be described as follows. The earliest DAS_1 (0.11 ps), resembling the shape of the overall TA signal, mostly represents a non-radiative relaxation mechanism bringing the CDs back to the ground state, inherent to the CDs themselves. Next, DAS_2 (1.06 ps) and DAS_3 (20 ps) mostly appear as a continuum-like ESA signal spanning most of the probed wavelength, accompanied by a negative dip close to the

pump wavelength, associated to a contribution from the GSB signal. In the literature,[21] signals of this kind have been associated to electrons populating the conduction band of the system, being thus able to explore a continuum of energy states, explaining the broad and spectrally flat ESA. Therefore, these DAS describe the decay back to the ground state of electrons which have been promoted to the conduction band of the CDs core. In addition, the weak ESA bands found in the DAS decaying in 20 ps are probably due to transitions which bring electrons from surface-associated emissive states back to the core. Non radiative transitions such as the ones observed here are not uncommon for carbon dots; for example, deep-UV excitation of CDs is considered to cause π–π* (and n-π*) transitions which then lead to dark states not contributing to the overall emission.[22] Lastly, the longest lived DAS_4 ($\tau > 1$ ns) equals the TA spectrum at long times. This is the TA spectrum of CDs after the end of picosecond and sub-picosecond relaxations, i.e. it represents the CDs which are later observed though nano-second time-resolved spectroscopy and steady-state spectroscopy.

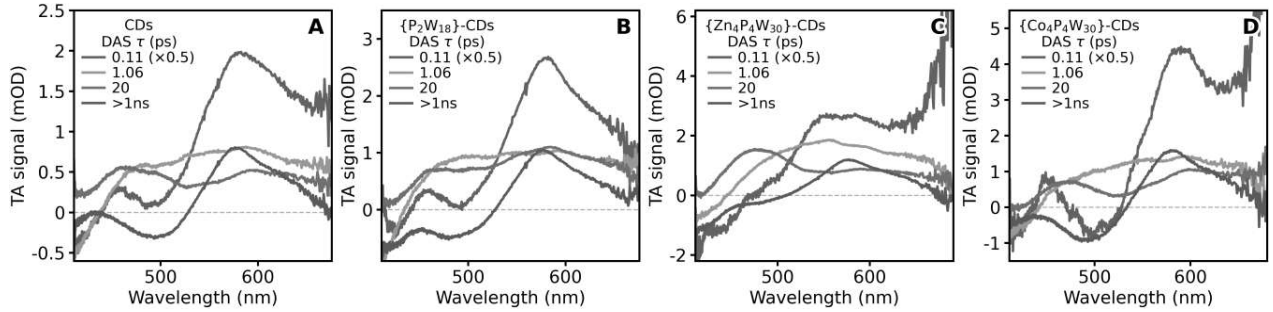

Figure 5: The four decay associated spectra (DAS) observed in the TA signal of A) CDs, B) $\{P_2W_{18}\}$-CDs complexes, C) $\{Zn_4P_4W_{30}\}$, and D) $\{Co_4P_4W_{30}\}$; samples obtained at a 1.25μM polyoxometalate concentration; the lifetime associated to each DAS is indicated.

As already mentioned, the fitting procedure ensures that data obtained both in the absence and presence of POMs can always be described by the same lifetimes, despite the clear evidence of excited-state quenching from steady-state data. From this we can conclude that the POM-CDs interactions responsible of fluorescence quenching must occur on a time-scale shorter than the time resolution of the performed TA experiments (100 fs). This conclusion is confirmed by Figure 6, where we compare the spectra at

short delays (0.24 ps) and long delays (as represented by DAS_4) between bare CDs and the different POM-CDs hybrids. In this plot, the spectra are compared after normalization on the longest-wavelength ESA signal, which shows similar shape in all cases. We see that strong differences in the signals are clearly present since the very beginning of the observation, which confirms that the processes causing fluorescence quenching must have occurred on a time-scale faster than that measurable by the TA setup.

To gain further insight on the nature of these processes, we first discuss the case of $\{P_2W_{18}\}$ (Figure 6A and 6D) and $\{Zn_4P_4W_{30}\}$ (Figure 6B and 6E). Here, we see that the interaction of CDs with the POM causes an imbalance between the GSB and SE component, whereby the former is enhanced and the latter decreases. If we compare TA signals of bare CDs at short and long times, we also see that the GSB component undergoes a strong decay due to electron-hole recombination. In contrast, such an effect is almost absent in POM-CDs hybrids. Therefore, the GSB enhancement upon POM addition becomes especially clear at a long-time delay (Figure 6D and 6E). These changes can be read as the spectral signature of an electron transfer between CDs and both $\{P_2W_{18}\}$ and $\{Zn_4P_4W_{30}\}$ POMs: as the photoexcited electrons are transferred from CDs to POMs, the ground state cannot be repopulated anymore. Therefore, the GSB signal in these POM-CDs nanohybrides lacks any relaxation and its intensity is preserved until long time delays. In parallel, the decrease of stimulated emission is a clear indication of the occurring quenching, since this band is directly related to the sample photoluminescence. As already mentioned, the time scale of this electron transfer must be faster than our temporal resolution (< 100 fs), because the changes in the shape of the TA signal are already present at the earliest delays, and the time scales extracted from the fits are identical in all samples. Interestingly, the differences between the TA spectra of CDs and POM-CDs persist till the end of the explored temporal range, additionally indicating that no back-electron transfer occurs within at least the first 200 ps from photoexcitation. Finally, as at the end of the transfer process the POMs are in a reduced state, it would be expected to observe the rise of a related spectral signature. Unfortunately, no further evidence of POMs photoreduction can be directly observed, because the related spectral features are found outside the

wavelength range which our TA setup allows to probe; for instance, reduced $\{P_2W_{18}\}$ displays absorption bands found either below 300 nm or above 650 nm.[23]

Additional considerations must be made to explain what happens in the presence of $\{Co_4P_4W_{30}\}$ (Figure 6C and 6F), where we see a different behavior. Also in this case, when compared to bare CDs, we observe changes in the spectral region of the GSB, but these are much smaller than for the other two POMs, and not accompanied by a disappearance of the SE. This evidence suggests a different mechanism operating for $\{Co_4P_4W_{30}\}$-CDs hybrids, as opposed to the other two POMs. In fact, the overall shape of the TA signal in $\{Co_4P_4W_{30}\}$-CDs composites remains much closer to bare CDs than observed for the other two POMs, leading to only a minor imbalance between GSB and SE components. Considering that $\{Co_4P_4W_{30}\}$ displays a significant absorption in the 400-500 nm region (Figure 2C and S1), which overlaps with CD fluorescence, photo-excited CDs might in principle undergo an energy transfer towards $\{Co_4P_4W_{30}\}$, as an alternative to electron transfer which is the only possibility for the other two POMs. Indeed, an energy transfer would equally affect both the GSB and the SE components of the TA signal of $\{Co_4P_4W_{30}\}$-CDs hybrids, consistent with the lack of the GSB-SE imbalance found in the other two POMs. On the other hand, an energy transfer to $\{Co_4P_4W_{30}\}$ should lead to the appearance of the spectral signature of photoexcited POMs in the TA spectra.

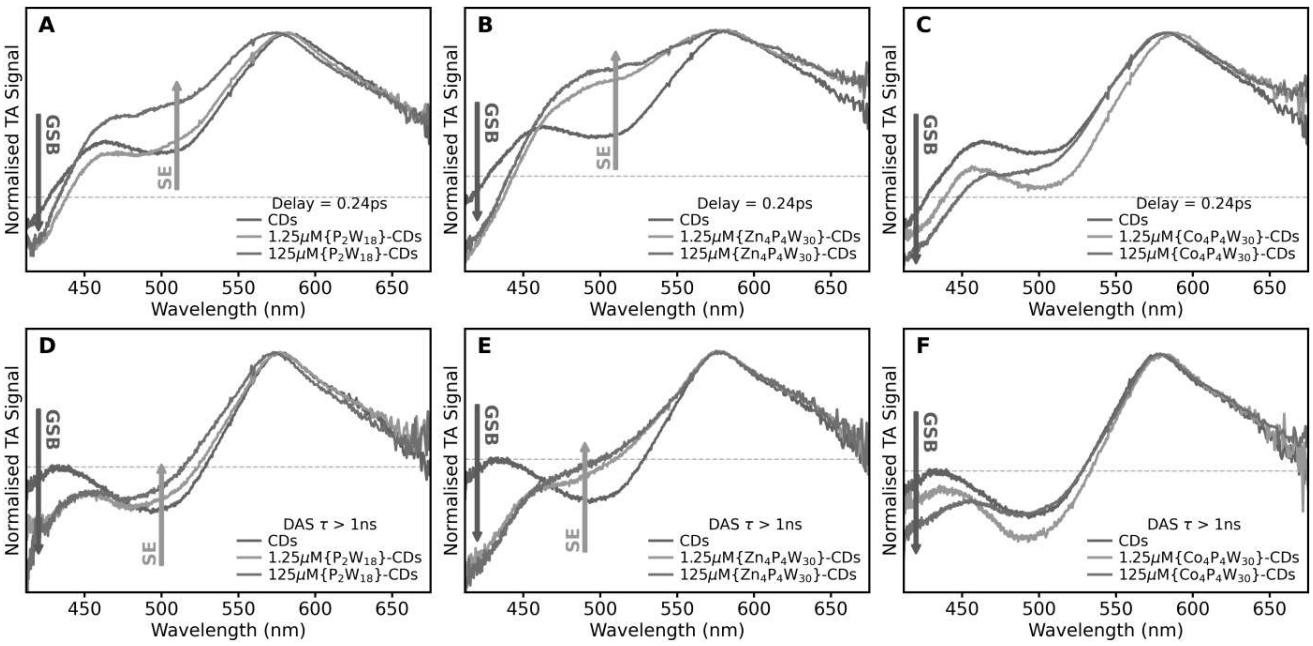

Figure 6: Comparison between the ultrafast transient absorption spectra at a delay of 0.24 ps from excitation (A, B and C) and between the longest-lived (τ > 1ns) DAS associated to the signals of CDs (D, E and F) in the absence and presence of POMs at concentrations of 1.25 μM and 125 μM; the comparisons are relative to the presence of polyoxometalate $\{P_2W_{18}\}$ (A and D), $\{Zn_4P_4W_{30}\}$ (B and E) and $\{Co_4P_4W_{30}\}$ (C and F).

To verify the last point, we consider the difference between the TA signal of $\{Co_4P_4W_{30}\}$-CDs complexes and that of bare CDs, as obtained at a POM concentration equal to 125 μM, which is plotted in Figure 7 at different delays. This signal is mostly negative, with two main components peaking below 500 nm and the other found close to 560 nm. It appears instantaneously and then undergoes an evolution over a time scale of several picoseconds, which can be described by time scales of 1.47 ± 0.02 ps and 24.6 ± 0.4 ps, as obtained from a global fit shown in Figure S5. Unfortunately, these timescales are very close to the one recorded on the original data, so it is very difficult to isolate them from the previous fitting procedure. Most interestingly, at long delays from excitation, the resulting spectra fairly match the steady-state absorption of $\{Co_4P_4W_{30}\}$, inverted in sign. Therefore, these difference spectra can be clearly interpreted as the appearance of the GSB of photoexcited $\{Co_4P_4W_{30}\}$. This result can be taken as the

spectral signature of the production of photoexcited $\{Co_4P_4W_{30}\}$ due to ultrafast energy transfer from CDs, occurring also in this case within our temporal resolution of 100 fs and leading to the population of excited POMs. A control experiment done on pure $\{Co_4P_4W_{30}\}$ in the same conditions leads to a lack of any measured TA signal, ruling out the possibility that the appearance of their GSB signal is due to their direct photoexcitation, and therefore supporting again the energy transfer from CDs. Indeed, a direct excitation of $\{Co_4P_4W_{30}\}$ remains very inefficient even at the highest explored concentration (125 µM) because of the relatively low absorption at 400 nm, in contrast to the very high absorption efficiency of CDs in this region which allows them to act as efficient photosensitizers for POMs.

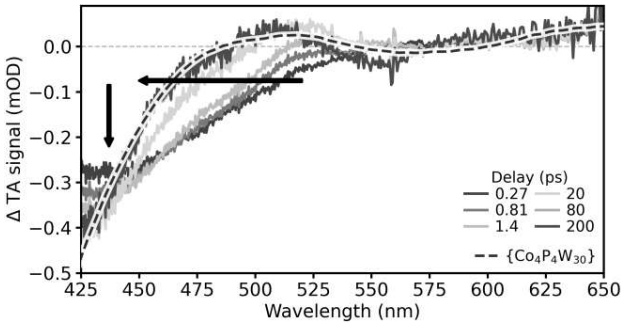

Figure 7: Spectra at different delays from excitation obtained as difference between the TA signal of $\{Co_4P_4W_{30}\}$-CDs complexes obtained at a 125 µM $\{Co_4P_4W_{30}\}$ concentration and the TA signal of CDs; arrows indicate the evolution direction of the signal; the dashed curve represents the steady-state absorption of $\{Co_4P_4W_{30}\}$ which overlaps the TA difference at long delays from excitation.

While this result clearly demonstrates that the interaction between CDs and $\{Co_4P_4W_{30}\}$ at high concentration (125 µM) is driven by energy transfer, the result is less straightforward at low POM concentrations (1.25 µM). In fact, when trying to calculate the same difference spectra using the $\{Co_4P_4W_{30}\}$-CDs sample obtained at low POM concentrations (1.25 µM) one cannot clearly isolate the spectral signature of photoexcited polyoxometalates (Figure S6). Thus, the data suggest that above a certain concentration threshold the interaction between CDs and this Co-based POM mainly occurs through an energy transfer mechanism, but a mixture of different processes takes place in the nanohybrid

formed at lower Co-POM concentration. Because of CDs ability to undergo both an electron transfer — as in the case of $\{P_2W_{18}\}$ and $\{Zn_4P_4W_{30}\}$ — and an energy transfer, we believe the complexity of the observed data is due to multiple mechanisms occurring at the same time.

Conclusions

We reported a simple route to obtain CD-polyoxometalate complexes by exploiting highly efficient electrostatic interactions between the two species in solution phase, and we investigated in detail the electronic interactions within these nanohybrids through a variety of optical methods. Our result directly demonstrates strong ground- and excited-state interactions between CDs and tetranuclear Dawson-derived sandwich polyanions, as revealed by fluorescence quenching, changes in the steady-state optical absorption spectra, and by the results of femtosecond-resolved studies. However, the underlying mechanisms responsible for CD-POM interactions are found to vary among POMs. The presented results suggest that an electron transfer occurs from CDs towards both $\{P_2W_{18}\}$ and $\{Zn_4P_4W_{30}\}$ when the system is exposed to light irradiation, whereas an energy transfer is the main mechanism responsible for the interaction between CDs and $\{Co_4P_4W_{30}\}$. In all cases, the excitation transfer process occurs much faster than 1 ps and do not show any sign of reversal, such as back-electron transfer, even after hundreds of picoseconds. Therefore, our results highlight the extreme efficiency of CDs in behaving as sensitizers of all the POMs investigated, thus providing a very promising route to extend into the visible range the operational window to achieve photocatalysis with POMs.

While the tested polyoxometalates are in no way covering the whole range of existing POMs, we believe that our findings could be extended to more structures, paving the use to a broad range of future POM-CDs nanohybrids which may find their applications in multiple domains such as artificial photosynthesis and pollutants degradation.

Acknowledgments

This work was supported by the institutes Université de Paris and CNRS (Centre National de Recherche Scientifique) and University of Palermo. This project has received funding from the ANR (Agence

Nationale de la Recherche) (Project POMDOT, postdoctoral fellowship to M.M.-S.), the city of Paris (Project Emergence), Campus France and the Università Italo-Francese through project Galileo 2019 (PHC n° 42084ZF and Grant G19_72) and the European Union's Horizon 2020 research and innovation program under Marie Skłodowska-Curie Grant Agreement No 665850 (Ph.D. fellowship to A.M.).

References

(1) Höök, M.; Tang, X. Depletion of Fossil Fuels and Anthropogenic Climate Change—A Review. *Energy Policy* **2013**, *52*, 797–809. https://doi.org/10.1016/j.enpol.2012.10.046.

(2) Ramsurn, H.; Gupta, R. B. Nanotechnology in Solar and Biofuels. *ACS Sustainable Chem. Eng.* **2013**, *1* (7), 779–797. https://doi.org/10.1021/sc400046y.

(3) Sorensen (Sorensen), B. *Solar Energy Storage*; Academic Press, 2015.

(4) Zhang, S. S. Problem, Status, and Possible Solutions for Lithium Metal Anode of Rechargeable Batteries. *ACS Appl. Energy Mater.* **2018**, *1* (3), 910–920. https://doi.org/10.1021/acsaem.8b00055.

(5) Chen, D.; Cheng, Y.; Zhou, N.; Chen, P.; Wang, Y.; Li, K.; Huo, S.; Cheng, P.; Peng, P.; Zhang, R.; Wang, L.; Liu, H.; Liu, Y.; Ruan, R. Photocatalytic Degradation of Organic Pollutants Using TiO2-Based Photocatalysts: A Review. *Journal of Cleaner Production* **2020**, *268*, 121725. https://doi.org/10.1016/j.jclepro.2020.121725.

(6) Joy, J.; Mathew, J.; George, S. C. Nanomaterials for Photoelectrochemical Water Splitting – Review. *International Journal of Hydrogen Energy* **2018**, *43* (10), 4804–4817. https://doi.org/10.1016/j.ijhydene.2018.01.099.

(7) Hisatomi, T.; Kubota, J.; Domen, K. Recent Advances in Semiconductors for Photocatalytic and Photoelectrochemical Water Splitting. *Chem. Soc. Rev.* **2014**, *43* (22), 7520–7535. https://doi.org/10.1039/C3CS60378D.

(8) Shon, J.-H.; Teets, T. S. Molecular Photosensitizers in Energy Research and Catalysis: Design Principles and Recent Developments. *ACS Energy Letters* **2019**. https://doi.org/10.1021/acsenergylett.8b02388.

(9) Kawawaki, T.; Negishi, Y.; Kawasaki, H. Photo/Electrocatalysis and Photosensitization Using Metal Nanoclusters for Green Energy and Medical Applications. *Nanoscale Adv.* **2020**, *2* (1), 17–36. https://doi.org/10.1039/C9NA00583H.

(10) Lim, S. Y.; Shen, W.; Gao, Z. Carbon Quantum Dots and Their Applications. *Chem. Soc. Rev.* **2015**, *44* (1), 362–381. https://doi.org/10.1039/C4CS00269E.

(11) Wang, X.; Cao, L.; Lu, F.; Meziani, M. J.; Li, H.; Qi, G.; Zhou, B.; Harruff, B. A.; Kermarrec, F.; Sun, Y.-P. Photoinduced Electron Transfers with Carbon Dots. *Chem. Commun.* **2009**, No. 25, 3774. https://doi.org/10.1039/b906252a.

(12) Cadranel, A.; Margraf, J. T.; Strauss, V.; Clark, T.; Guldi, D. M. Carbon Nanodots for Charge-Transfer Processes. *Acc. Chem. Res.* **2019**, *52* (4), 955–963. https://doi.org/10.1021/acs.accounts.8b00673.

(13) M. Cameron, J.; J. Wales, D.; N. Newton, G. Shining a Light on the Photo-Sensitisation of Organic–Inorganic Hybrid Polyoxometalates. *Dalton Transactions* **2018**, *47* (15), 5120–5136. https://doi.org/10.1039/C8DT00400E.

(14) Madonia, A.; Martin-Sabi, M.; Sciortino, A.; Agnello, S.; Cannas, M.; Ammar, S.; Messina, F.; Schaming, D. Highly Efficient Electron Transfer in a Carbon Dot–Polyoxometalate Nanohybrid. *J. Phys. Chem. Lett.* **2020**, *11* (11), 4379–4384. https://doi.org/10.1021/acs.jpclett.0c01078.

(15) Long, D.-L.; Tsunashima, R.; Cronin, L. Polyoxometalates: Building Blocks for Functional Nanoscale Systems. *Angew. Chem. Int. Ed.* **2010**, *49* (10), 1736–1758. https://doi.org/10.1002/anie.200902483.

(16) Wang, L.; Wang, Y.; Xu, T.; Liao, H.; Yao, C.; Liu, Y.; Li, Z.; Chen, Z.; Pan, D.; Sun, L.; Wu, M. Gram-Scale Synthesis of Single-Crystalline Graphene Quantum Dots with Superior Optical Properties. *Nat. Commun.* **2014**, *5* (40), 5357–5365. https://doi.org/10.1038/ncomms6357.

(17) Contant, R.; Klemperer, W. G.; Yaghi, O. Potassium Octadecatungstodiphosphates(V) and Related Lacunary Compounds. In *Inorganic Syntheses*; John Wiley & Sons, Ltd, 2007; pp 104–111. https://doi.org/10.1002/9780470132586.ch18.

(18) Finke, R. G.; Droege, M. W.; Domaille, P. J. Trivacant Heteropolytungstate Derivatives. 3. Rational Syntheses, Characterization, Two-Dimensional Tungsten-183 NMR, and Properties of Tungstometallophosphates P2W18M4(H2O)2O6810- and P4W30M4(H2O)2O11216- (M = Cobalt, Copper, Zinc). *Inorg. Chem.* **1987**, *26* (23), 3886–3896. https://doi.org/10.1021/ic00270a014.

(19) Lakowicz, J. R. *Principles of Fluorescence Spectroscopy*, 3rd ed.; Springer: New York, 2006.

(20) Sciortino, A.; Madonia, A.; Gazzetto, M.; Sciortino, L.; Rohwer, E. J.; Feurer, T.; Gelardi, F. M.; Cannas, M.; Cannizzo, A.; Messina, F. The Interaction of Photoexcited Carbon Nanodots with Metal Ions Disclosed down to the Femtosecond Scale. *Nanoscale* **2017**, *9* (33), 11902–11911. https://doi.org/10.1039/C7NR03754F.

(21) Sciortino, A.; Gazzetto, M.; Soriano, M. L.; Cannas, M.; Cárdenas, S.; Cannizzo, A.; Messina, F. Ultrafast Spectroscopic Investigation on Fluorescent Carbon Nanodots: The Role of Passivation. *Phys. Chem. Chem. Phys.* **2019**, *21* (30), 16459–16467. https://doi.org/10.1039/C9CP03063H.

(22) Demchenko, A. P. Excitons in Carbonic Nanostructures. *C* **2019**, *5* (4), 71. https://doi.org/10.3390/c5040071.

(23) Varga, G. M.; Papaconstantinou, E.; Pope, M. T. Heteropoly Blues. IV. Spectroscopic and Magnetic Properties of Some Reduced Polytungstates. *Inorg. Chem.* **1970**, *9* (3), 662–667. https://doi.org/10.1021/ic50085a045.